ELSEVIER

Contents lists available at ScienceDirect

Journal of Membrane Science

journal homepage: www.elsevier.com/locate/memsci



Polyvinyl chloride (PVC) ultrafiltration membrane fouling and defouling behavior: EDLVO theory and interface adhesion force analysis



Wanyi Fu^{a,1}, Lan Wang^{b,1}, Fangjuan Chen^b, Xuezhi Zhang^{b,*}, Wen Zhang^{a,*}

- ^a John A. Reif, Jr. Department of Civil and Environmental Engineering, New Jersey Institute of Technology, Newark, NJ 07102, USA
- b Center for Microalgal Biotechnology and Biofuels, Institute of Hydrobiology, Chinese Academy of Sciences, Wuhan 430061, China

ARTICLE INFO

Keywords: Membrane fouling EDLVO theory Adhesion force Defouling kinetics AFM

ABSTRACT

To unravel fouling and defouling mechanisms of protein, saccharides and natural organic matters (NOM) on polymeric membrane during filtration, this study investigated filtration characteristics on polyvinyl chloride (PVC) ultrafiltration membranes with bovine serum albumin, dextran, humic acid as model foulants. Membrane fouling and defouling performances were analyzed through monitoring the flux decline during filtration and flux recovery during physical backwash. Physico-chemical properties (e.g., hydrophobicity and surface charge) of PVC membrane and foulants were characterized, which were used in the extended Derjaguin–Landau–Verwey–Overbeek (EDLVO) theory to calculate the interaction energies between membrane-foulant and foulant-foulant. The results showed that at the later filtration stages the fouling rate was strongly correlated with the deposition rate, which was determined by the interaction energy profile calculated by EDLVO. Moreover, the adhesion forces of membrane–foulant and foulant–foulant were further measured by atomic force microscopy (AFM) with modified colloidal probes. A positive correlation ($R^2 = 0.845$) between particle detachment rate (determined by adhesion force) and defouling rate was developed for BSA and HA foulants that led to cake layer formation. By contrast, dextran defouling rate was off this correlation as dextran partially clogged membrane pores due to its smaller size.

1. Introduction

Membrane fouling has been a limiting factor for membrane filtration in diverse applications in separation, water and wastewater treatment [1–4]. Membrane fouling is primarily attributed to membrane–foulant interactions followed by subsequent foulant–foulant interactions [5–7]. Interfacial properties of both membranes and foulants have important impacts on membrane fouling kinetics and fouling removal or defouling [8,9]. Therefore, the delineation of the membrane–foulant or foulant–foulant interaction mechanisms are critical to understanding their roles in membrane fouling and defouling processes.

Most previous studies examined bulk scale membrane fouling behavior and evaluations, such as filtration resistance, flux decline rate and flux recovery ratio [10–12]. However, both membrane and foulants properties greatly impact membrane filtration performance. These properties include foulant molecular weight, zeta potential, colloidal size, membrane surface zeta potential, hydrophobicity and surface roughness [13–16]. Particularly, previous studies have reported the influences of surface hydrophobicity and charge on membrane fouling

[17,18]. Atomic force microscopy (AFM) has widely been used to characterize pristine and fouled membrane surfaces [19,20]. In addition to surface morphology mapping, quantification of interaction forces by AFM greatly aids the understanding of membrane fouling mechanisms [6,21,22]. For example, interaction forces between polymeric membranes and AFM probes coated with foulants of humic acid (HA) and bovine serum albumin (BSA) provided insight into the foulant-membrane interactions and fouling propensity [21,23]. Mi et al. observed the important role of foulant-foulant adhesion force in determining the organic fouling rate during forward osmosis membrane processes [22]. Meng et al. reported that high membrane-HA adhesion forces caused fast deposition of the HA onto the membrane surface, leading to severe membrane fouling in the initial filtration stage [5]. However, we hypothesize that adhesion forces govern defouling propensity instead of fouling potential as reported previously [5,22], because adhesion only occurs when chemical bonds form between membrane and foulants. Therefore, adhesion forces should be used to establish correlation with defouling kinetics. Clearly, further quantitative investigations of fouling, defouling processes, and contribution

^{*} Corresponding authors.

E-mail addresses: zhangxuezhi@ihb.ac.cn (X. Zhang), wzhang81@njit.edu (W. Zhang).

¹ These authors contributed equally to this work.

from interfacial forces will provide new insight into the prevention of membrane fouling and rationale design of antifouling membrane filtration processes.

In this study, the fouling and defouling kinetics of polyvinyl chloride (PVC) ultrafiltration membrane were investigated. Dextran (DEX), humic acid (HA) and bovine serum albumin (BSA) were used as model foulants, representative of polysaccharides, natural organic matters and proteins, respectively [24,25]. These model foulants are commonly reported to have detrimental effects on membrane filtration and lead to membrane fouling. The interaction forces involved at the membrane-foulant and foulant-foulant interfaces were measured by AFM to analyze the roles of interfacial forces in fouling and defouling processes. For the first time the fouling or defouling kinetics was analyzed separately for the initial and later stages of filtration, where foulant-membrane interactions and foulant-foulant interactions may jointly play a role. Accordingly, we applied the Maxwell model or Maxwell approach to calculate foulant deposition rate that was correlated with fouling rate or flux decline rate [26]. By contrast, adhesion forces were used to establish correlation with defouling kinetics based on a particle transport model.

2. Method and materials

2.1. Organic foulants

Polysaccharide, protein and humic acid are common membrane foulants known to cause membrane fouling [27,28]. Commercial protein (BSA) (Beijing Jiangchen Biotech Co., $M_w=66.45\,\mathrm{kDa}$, China), dextran (DEX) (Aladdin, $M_w=70\,\mathrm{kDa}$, China) and humic acid (HA) (Sigma Aldrich, USA) were used to prepare stock feed solutions. Ultrapure Milli-Q water (18.2 M Ω cm at 25 °C, Direct-Q* UV3 System, EMD Millipore, Bedford, MA, USA) was used for the preparation of solutions. The concentrations of these stock solutions were: 1 g-BSA L⁻¹, 0.83 g-DEX L⁻¹, and 4.45 g-HA L⁻¹, respectively, which yield the same level of TOC at 280 mg L⁻¹. The HA solution was filtered with 0.45 μ m membranes (cellulose nitrate membrane filters, Whatman) to remove the insoluble particles. All the solutions were stored at 4 °C prior to use.

2.2. Ultrafiltration membranes

Hollow fiber PVC membranes were purchased from Hainan Litree Purifying Technology Co. Ltd. The membrane has a MWCO of 50 kDa. SEM images of the cross-section and surface structure of the membrane were shown in Fig. S1a-b. One fiber was then cut into 0.2 m in length and placed into a transparent plastic tubing to make a single fiber module. The effective membrane surface area was approximately 6.28 cm² per module. Prior to the experiment, virgin membranes were rinsed carefully to remove preservatives and soaked in deionized water for 24 h to remove impurities [29].

2.3. Filtration experiments

A laboratory-scale filtration system was assembled for membrane filtration experiments (Fig. S2). A membrane filtration unit with automatic TMP adjusting (Spectrum Laboratories, Inc.) was used for the fouling test. The membrane was backwashed using air assistant backwashing developed previously, which involves backwashing with air in the permeate side, and flushing with air and pure water in the feed side of the membrane [30]. An electronic balance (Mettler Toledo, Inc.) and WinWedge software (TAL Technologies, Inc.) were used to continuously monitor the permeate weight to calculate the permeate flux change. The clean water tests were conducted to determine the filtration performance at different TMPs as shown in Fig. S2b. Filtration experiments generally consisted of the following steps. Firstly, the membrane was filtered with DI water under 48 kPa TMP for 1 h to reach a relatively stable flux. Then, the TMP was increased to 100 kPa to establish a stable

water permeate flux named J_0 . Next, the fouling experiment was conducted at 100 kPa under a cross flow velocity of $0.3 \,\mathrm{m\,s^{-1}}$ by filtering the stock solutions of BSA, DEX or HA, respectively. After every 15 minutes' filtration, the membrane was backwashed with 30 mL DI water for 5 min. The total filtration time was 150 min (10 cycles) and each filtration experiment was repeated for 3 times.

The permeate flux, J (L m⁻² h⁻¹) is calculated by:

$$J = \frac{\Delta m}{\rho \cdot \Delta t \cdot A} \times 1000 \tag{1}$$

where J is the permeate flux (L m⁻² h⁻¹, LMH); Δm (kg) is the mass of permeate measured in filtration duration time Δt (h); ρ is the density of permeate (kg m⁻³); A is the filtration area (m²).

The normalized flux J^* (dimensionless) is defined as the ratio of the actual flux J and the maximum or initial membrane flux J_0 :

$$J^* = \frac{J}{J_0} \tag{2}$$

The flux decline rate was calculated to indicate the fouling rate (min⁻¹):

$$\frac{\mathrm{d}J^*}{\mathrm{d}t} = \frac{|J_n^* - J_{0,n}^*|/J_{0,n}^*}{\Delta t_f} \tag{3}$$

where n is the cycle number; $J_{0,n}^*$ was the initial permeate flux of the n cycle; J_n^* was the permeate flux at the end of the n cycle; Δt_f is the filtration time in each cycle.

The flux recovery ratio was calculated by:

Flux recovery ratio (%) =
$$\frac{J_{0,n+1}^*}{J_{0,n}^*} \times 100$$
 (4)

where n is the cycle number; $J_{0,n}^*$ was the initial flux of the permeate of the n cycle; $J_{0,n+1}^*$ was the initial flux of the permeate of the (n+1) cycle.

The flux recovery rate (defouling rate) was calculated by:

Defouling rate
$$\frac{dJ^d}{dt} = \frac{(J_{0,n}^* - J_{15,n-1}^*)/J_{15,n-1}^*}{\Delta t_b}$$
 (5)

where $J_{0,n}^*$ was the initial flux of the permeate of the n cycle; $J_{15,n-1}^*$ was the flux before the backwashing at the n-1 cycle; Δt_b is the backwashing time during each cycle.

2.4. Characterization of membranes and foulants

Contact angle measurements of membranes and foulants were conducted on an optical contact angle goniometer (JC2000DM, Powereach, Shanghai, China). The surface zeta potential of membrane, zeta potential and hydrodynamic sizes of foulants were measured on a dynamic light scattering (DLS) instrument (ZetaSizer Nano ZS, Malvern Instruments), and the procedures were detailed in our previous work [9]. Confocal laser scanning microscopy (CLSM; Leica TCS SP8 Confocal Spectral Microscope Imaging System, GmbH, Germany) was employed to analyze the fouling distribution on PVC membranes at both inner surface and cross-section surfaces perspective. The details of the characterization methods above are provided in Section S1.

2.5. Calculation of interaction energy and surface deposition rate based on EDLVO theory

The extended Derjaguin Landau Verwey Overbeek (EDLVO) theory has been widely used to demonstrate the contributions of surface properties of membranes or foulants to colloidal interactions and fouling potential on membrane filters [31–33]. In this study, the membrane-foulant interactions were modeled as surface–particle geometry while foulant-foulant interactions were particle-particle geometry. The total interaction energies, U_{Total} , of membrane-foulant and

foulant-foulant systems consist of the Lifshitz–van der Waals (vdW), U_{vdW} , electrostatic double-layer (EL), U_{EL} and Lewis acid–base (AB) energy, U_{AB} [33,34]. Detailed calculations of each interaction energy component were reported in our previous papers [9,35].

To further explain the effect of interaction energy barrier on membrane fouling prediction, the surface deposition rate $(\frac{dn}{dt})$ was derived from the Smoluchowski's population balance equation [36]:

$$\frac{\mathrm{d}n}{\mathrm{d}t} \approx \frac{1}{2}\alpha\beta n\tag{6}$$

where α is the collision efficiency, β is the collision frequency, n is the number concentration of particles.

The collision efficiency (α) can be solved with the Maxwell approach [26]:

$$\alpha = \delta \cdot \int_{E_h}^{\infty} e^{-E} E^{1/2} dE \tag{7}$$

where δ is the hydrodynamic damping factor (also called the drag effect factor, dimensionless), which is taken as 1. E_b is the interaction energy barrier (k_BT), obtained from the interaction energy profiles as shown in Fig. S3, and E is the random kinetic energy (k_BT) of foulants.

The collision frequency (β) of foulant particles against membrane surface is expressed as [36,37]:

$$\beta = \frac{8k_B T}{3\mu} \left[2 \int_0^\infty \lambda(u) \frac{\exp(U_{vwd}(h)/k_B T)}{(2+u)^2} du \right]^{-1}$$
 (8)

where U_{vwd} is the van der Waals forces interaction energy calculated by the EDLVO theory; k_B is the Boltzmann constant; T is the absolute temperature; μ is the viscosity of the solution $(1 \times 10^{-3} \text{ Pa s})$; h is separation distance between two particles (nm) or between particle and surface (nm); and $\lambda(u)$ is the correction factor for the diffusion coefficient. The detailed calculation procedures are provided in the Section S8.

2.6. Measurement of foulant-foulant and foulant-membrane adhesion forces by AFM

The probe used in the AFM force measurements was commercial tipless silicon nitride probe (MLCT-O10, Bruker, America) with spring constant of 0.1 N m⁻¹. Firstly, a polystyrene microsphere (10 µm diameter) was attached by a small drop of two-component epoxy resin (1:1) to the end of the probe. Then, the prepared probe was left at room temperature for at least 12 h to guarantee the solidity of the epoxy resin. The foulant-coated colloidal probes were fabricated by immersing the prepared colloidal probes into BSA, DEX and HA solutions (identical to that in the corresponding fouling experiments) for 24 h at 4 °C to reach adsorption equilibrium [5]. Fig. S1c-d are the SEM images that were acquired on the field emission scanning electron microscope (FESEM, LEO 1530 VP, Oberkochen, Germany) to show the unmodified and modified AFM colloidal probes. All AFM force measurements were carried out in a Petri dish with DI water using contact mode at the oscillation frequency of 1.03 Hz and the initial loading force of 5.0 nN. Each membrane sample was cut into flat sheets and then mounted onto a Petri dish bottom with double-sided adhesive tape. Each interaction force measurement was done at 15 spots and 20-30 curves for each spot depending on the repeatability of measurement results.

3. Results and discussion

3.1. Characterization of membranes and foulants

The characteristics of foulants and membranes were summarized in Table 1. BSA and HA had mean hydrodynamic diameters of 266 and 213 nm respectively, which were greater than that of DEX. In aqueous solutions, humic acid and proteins usually aggregate together and form colloidal clusters of tens or hundreds of nanometers in size [5,8,38].

Zeta potentials of BSA and HA in their stock solution were also greater in magnitude than that of DEX. These parameters are used for the calculations of interaction energy, foulant deposition rate and detachment rate in the following sections.

3.2. Fouling kinetics for different foulants on PVC membranes

Fig. 1 shows the permeate flux changes during the filtration of BSA, DEX and HA solutions. The initial absolute fluxes for different foulants under the same TMP were much lower than the initial flux when filtering DI water (460 LMH at TMP 100 kPa), indicating that the fouling may occur instantly within the few seconds of filtration. The degree of fouling also depends on the differences of foulant types, concentrations, and foulant-membrane interactions [43-45]. For example, the foulant solution was prepared with the same level of TOC (280 mg L⁻¹) and the foulant concentrations were: 1 g-BSA L⁻¹, 0.83 g-DEX L⁻¹, and 4.45 g-HA L⁻¹, respectively. HA was clearly added at a higher concentration than the other two foulants and therefore caused a quicker membrane clogging and fouling than DEX or BSA. Given that the hydrodynamic size of HA is also greater than DEX, the HA-induced fouling should be more pronounced than DEX due to a rapid cake layer formation. To compare the fouling kinetics resulted from different foulant types, the normalized fluxes are plotted in Fig. 1b. The flux change in each filtration cycle was similar with a fast flux decline in the first two minutes and followed by a relatively slow decrease. Thus, the first filtration cycle in Fig. 1b was extracted to better exhibit the potential turning point during fouling (Fig. 1c), which was also used to analyze the fouling rates during filtrations of different foulants.

For those three foulants, the flux decline rates calculated by Eq. (3) were different during the initial (the first two minutes in the cycle) and later filtration stages (after two minutes in the cycle). During the initial filtration period, the filtration flux decreased more rapidly and the flux decline rates (fouling kinetics) followed the order: BSA > HA > DEX (Fig. 1c). At the later filtration stage, the flux decline rate slowed down and generally followed the order: DEX > BSA > HA. Clearly, membrane fouling processes are likely affected by various factors such as physicochemical properties of foulants and membranes and surface interaction characteristics (foulant-membrane and foulant-foulant) [5–7], which result in different fouling behaviors or fouling mechanisms [46,47].

Because the cluster size of BSA was greater than the pore size, BSA molecules were rejected by membrane pores, accumulated on the membrane surface and subsequently formed a cake layer as evidenced with CLSM in Figs. S3b and S3d. The cake layer blocks the pores and reduces permeate flux sharply at the initial stage. In comparison, the permeate flux decline rate for DEX was relatively slower than that of BSA. As DEX has a smaller particle size (26 \pm 6 nm) and the membrane pores may be blocked by DEX gradually. This is also indicated by the confocal images obtained by CLSM in Fig. S4a, which showed white colored and snowflakes-like materials on DEX fouled membrane surface. By contrast, BSA (Fig. S4b) was compactly distributed on the surface of BSA-fouled membrane. Additionally, BSA is more hydrophobic than DEX, and thus, the hydrophobic interactions could cause rapid binding and attachment of BSA on PVC membrane and thus a faster rate of fouling and flux decline than DEX in the beginning.

Fig. 1c shows that the fouling rate for the filtration of HA was between the rates of BSA and DEX. Since HA is not a homogeneous model organic matters, with molecular weights ranging from 2 kDa up to over 500 kDa [40,42], the fouling mechanism for HA could be a combination of pore blocking and a cake layer formation [48]. The large sized HA may deposit on the membrane surface and form a cake layer, whereas the small sized HA accumulates and blocks the pores. Fig. 1d shows that the flux decline rate in each cycle during the 150 min filtration of DEX decreased slightly while decline rates of BSA and HA slowed down abruptly after two filtration cycles and then stayed at a slower rate level than DEX. This phenomena could be explained by the differences in the

Table 1
Characteristics of the foulants and tested membrane.

Foulant	pH value	Hydrodynamic diameter/nm	Zeta potential in water/mV	Mass concentration/g L ⁻¹	Average molecular weight/g mol ⁻¹
Bovine Serum Albumin	8.0 ± 0.1	266 ± 20	- 22.1 ± 3.5	1.0	66,450
Dextran	8.2 ± 0.1	26 ± 6	- 16.4 ± 3.1	0.83	70,000
Humic Acid	7.9 ± 0.1	213 ± 13	-39.1 ± 1.8	4.45	4100 ^a /
Pristine PVC membrane	/	/	-46.1 ± 3.5^{b}	/	

Chin et al. [39]. According to previous literature, HA molecular weight range could be: 65% > 100 kDa [40]; 2-50 kDa [41]; or 2-500 kDa [42].

b Pristine PVC membrane was measured in 1 mM NaCl solutions with pH 8.0 \pm 0.1.

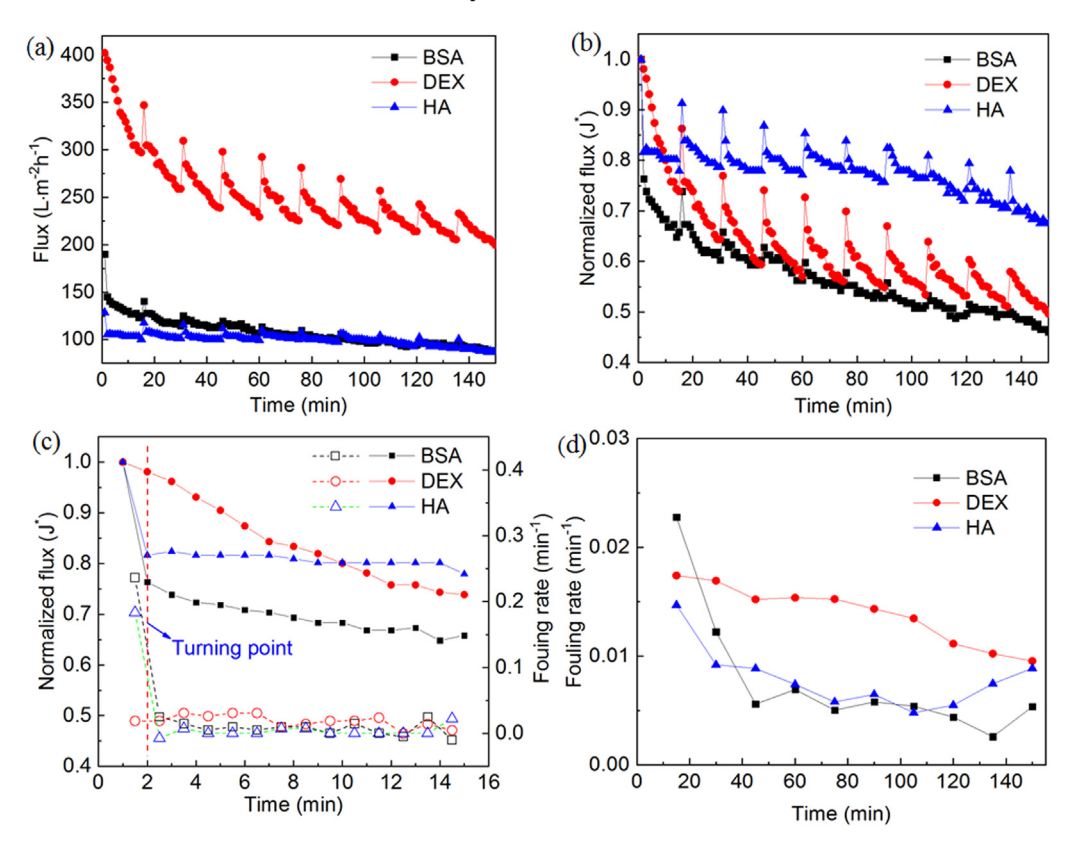


Fig. 1. (a) Absolute flux changes and (b) normalized flux decline curves for BSA, DEX and HA; (c) flux change with filtration time (solid dots) and the flux decline rate in different filtration stages (hollow dots) of the first filtration cycle; and (d) Flux decline rate for BSA, DEX and HA in each cycle.

fouling modes of DEX and HA or BSA. Fouling process could be affected by various factors such as physicochemical properties of foulants and membranes, operation conditions and solution chemistry [46]. Previous studies showed that the membrane-foulant and foulant-foulant interactions played an important role in the occurrence of membrane fouling and demonstrated that the EDLVO theory could partly explain membrane fouling behavior [5–7,47]. Therefore, both foulant-membrane and foulant-foulant interaction energies were calculated to predict the membrane behavior and fouling mechanism in the following sections.

$3.3. \ Interaction\ energy\ for\ membrane-foulant\ and\ foulant-foulant\ systems$

Fig. S3a shows the interaction energies between the PVC membranes and three foulants in DI water, which play decisive roles in the initial surface deposition (rate) of foulants on membrane. The energy barriers for the three foulant-membrane systems follow the order: ${\rm HA} > {\rm BSA} > {\rm DEX}$. A lower magnitude of energy barriers usually lowers the repulsion of foulant-membrane interaction and causes rapid deposition of foulants on membrane surface [8]. The fouling rate for these three foulants should follow the order: ${\rm DEX} > {\rm BSA} > {\rm HA}$, which partially agrees with the results of Fig. 1c. Fig. S3b shows the interaction energies between foulants themselves, which were considered in

the analysis of fouling kinetics in later filtration stage. Compared with the membrane-foulant interactions, the interaction energies were appreciably lower in magnitude for foulant-foulant interactions. The energy barriers followed the order: HA-HA > BSA-BSA > DEX-DEX, which is congruent with the fouling rate order (DEX > BSA > HA) during the later fouling stage (Fig. 1c). HA had the highest inter-molecular repulsion, whereas DEX had the lowest. As a result, a lower inter-foulant energy barrier clearly promotes foulant-foulant interaction and facilitates the formation of foulant layers, which increases the fouling tendency or rates (or a faster flux decline rate).

3.4. Correlation analysis between foulant deposition rate and fouling rate

Generally, a high interaction energy barrier reduces the tendency of colloidal interactions on membrane and thus prevents membrane fouling [49]. Fu et al. recently established a fouling kinetics model that incorporated the EDLVO theory into the particle transport equation [9]. This model indicated that the gradient of attractive interaction energy mediated the fouling rates of BSA or HA on polymer membranes. To further explain the effect of interaction energy barrier on membrane fouling prediction, the surface deposition rate $(\frac{dn}{dt})$ was derived from the Smoluchowski's population balance equation and the results were

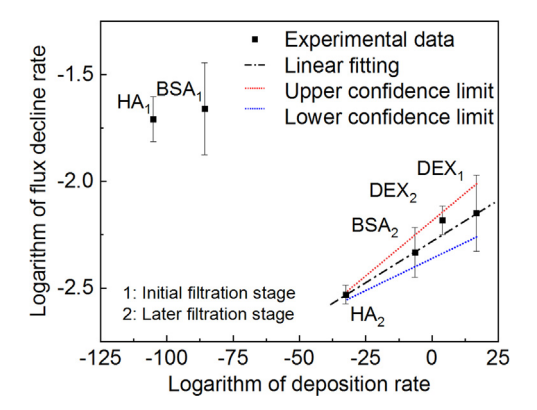


Fig. 2. The correlation between the logarithm of flux decline rate and the logarithm of deposition rate. The linear regression as well as the 95% prediction confidence are plotted.

presented in Section S3.

A linear regression between the deposition rate and the flux decline rate is established in Fig. 2. The linear fitting to experimental data was shown with 95% prediction confidence limits. All the filtration data at the later filtration stage fitted the linear regression curve, indicating that the model is suitable for the foulant-foulant interaction as the dominant fouling mechanism. The filtration data of BSA and HA at the initial filtration stage did not fit the linear regression. The actual flux decline rates were higher than that predicted by the linear fit. The BSA and HA foulants, due to their greater colloidal sizes than membrane pores, could swiftly form cake layers on the membrane surface and blocked the pores, which caused the rapid flux decline within only 2 min (Fig. 1c). After foulant layer formation, the foulant-foulant interaction began to dominate the fouling process. As a result, the flux decline rate was governed by the rate of foulant layer formation and layer characteristics (e.g., thickness and compressibility). The contribution from membrane-foulant interaction for BSA and HA could play a minor role in fouling resistance and flux decline.

Conversely, the fouling process by DEX was caused by pore narrowing due to the progressive surface deposition of DEX. The fouling rates or flux resistance varied with the dynamics of DEX deposition and was more influenced by membrane-foulant interaction forces until the membrane surface was fully covered by the DEX foulants. Therefore, the experimental data for DEX better fit our model for membrane fouling at initial filtration stage.

3.5. Defouling kinetics for different foulant-membrane systems

Fig. 3a shows the flux recovery ratio as defined in Eq. (4) in each filtration/backwash cycle. The flux recovery ratio for all foulants was lowest at the first cycle of filtration after 15 min, which means that most irreversible fouling occurred in the first cycle. The flux recovery ratios

for these three foulants were around 80% and stabilized after the third filtration cycle.

Fig. 3b shows the defouling rate as defined in Eq. (5) in each cycle as a measure of the flux recovery rate during the backwashing. DEX had a higher defouling rate than BSA and HA. Moreover, the defouling rate monotonically decreased with the filtration time for BSA and HA. However, DEX led to a peak of the defouling rate probably because the thicker and porous DEX-cake layer is easier to be flushed off the membrane surface than BSA or HA. The confocal images in Fig. S4a shows that membrane surface after 150 min filtration of DEX was covered by DEX, which is white colored and snowflakes-like materials. By contrast, BSA (green dots in Fig. S4b) was compactly distributed on the surface of BSA-fouled membrane. It is possible that BSA formed a denser cake layer, whereas HA formed a looser cake layer, which led to different fouling and defouling rates for BSA and HA. Other factors (layer thickness, porosity, and compressibility) may also vary the flux resistance and fouling/defouling characteristics.

Moreover, it was observed that DEX fouling is more severe than the one caused by HA and BSA (Fig. 1c), but it was to a large extent reversible by backwashing. Meanwhile, BSA fouling showed higher and increasing irreversibility and the periodic backwashing could not recover the flux effectively (Fig. 3b).

3.6. Adhesion force measurement for foulant-foulant and foulantmembrane systems

During the defouling process, the detached foulant must overcome the adhesion force between the membrane and the foulants or between the foulants themselves. Adhesion force is also called rupture force that is used to break the adhesive bonds. Fig. S5 illustrates the typical force-distance curve acquired by AFM and the relative frequency distributions of adhesion forces (also termed as cohesion for the identical interacting particles) between foulants and adhesion forces between foulants and PVC membranes. For each type of foulants, the adhesion forces of membrane-foulant are stronger than the corresponding adhesion forces of foulant-foulant.

The adhesion forces for PVC-BSA (-3.8 nN) is greater than PVC-HA (-0.03 nN), which supports the calculated defouling rate order (BSA < HA) in Fig. 3b. Likewise, the adhesion forces between foulant and foulant followed the order: BSA-BSA > HA-HA, which coincided with the defouling rate in later filtration/backwash cycles. High membrane-foulant adhesion forces are likely to cause irreversible fouling and low flux recovery ratio (Fig. 3a) as reported previously [38].

3.7. Correlation analysis between adhesion force and membrane defouling kinetics

The membrane defouling kinetics was delineated with the detachment rate based on the particle transport equation that we employed

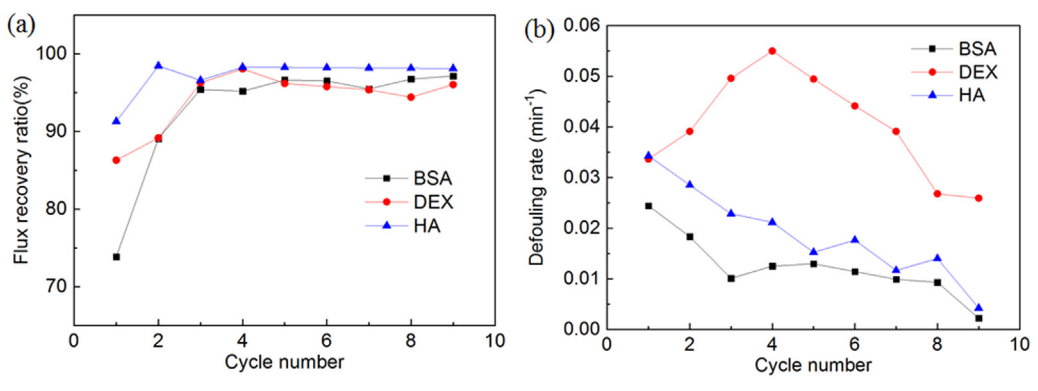


Fig. 3. Flux recovery ratios for BSA, DEX and HA (a) in each cycle and (b) flux recovery rate (defouling rate) curve for BSA, DEX and HA in each cycle.

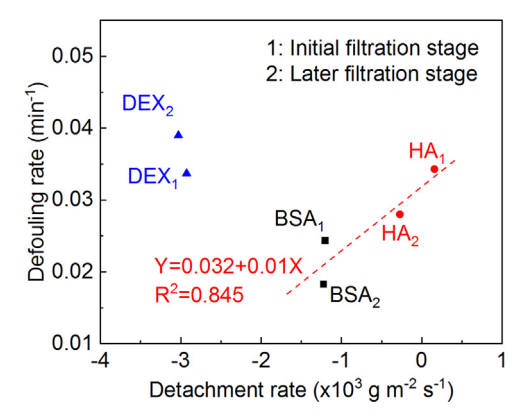


Fig. 4. Linear correlations analysis between detachment rate and defouling rate.

previously [37,50].

$$J_x = -D_x \frac{\partial C}{\partial x} + u_x C + \frac{D_x F_x C}{k_B T}$$
(9)

Where J_x is the particle flux, considered as the particle detachment rate (mg m⁻² s⁻¹) in this study, D_x is the diffusion coefficient (cm² s⁻¹), C is the particle concentration (mg m⁻³), u_x is the particle velocity components caused by the backwash water flow (m s⁻¹), F_x is the adhesion force between foulant-membrane or foulant-foulant (N). T is the temperature (K), k_B is the Boltzmann constant, 1.38×10^{-23} J K⁻¹.

The detailed calculations of diffusion, advection and interfacial adhesion force are provided in the Section S4. According to Eq. (9), the particle detachment rate is contributed by three components; and the comparisons of these components (Table S5) showed that, $J_{x(force)}$ was larger than $J_{x(diff)}$ and $J_{x(adve)}$. Particularly for BSA and DEX, $J_{x(diff)}$ and $J_{x(adve)}$ were substantially smaller by several orders of magnitude and thus could be negligible. Meanwhile the adhesion force for HA was almost 100-300 times smaller than BSA and DEX, the three components for HA were at the same order of magnitude. It is also interesting that these three components are all dependent on foulant saturated concentration and $J_{x(force)}$ is always greater than $J_{x(diff)}$ and $J_{x(adve)}$ under our experimental conditions. Our calculations show that only when the backwashing flux of BSA or DEX reach above approximately 1.1×10^5 – 3.5×10^5 LHM, $J_{x(adv)}$ can reach similar orders of magnitude as $J_{x(force)}$. However, typical backwashing flux commonly used for polymeric ultrafiltration membranes is between 7.5 LMH to 500 LHM [51,52]. It indicated that $J_{x(force)}$ is the dominating component for detachment rate, which is thus controlled by the adhesion force.

The calculated particle detachment rate and the defouling rate were plotted in Fig. 4, which yields a linear relationship ($R^2 = 0.845$) for BSA and HA filtration system. However, the experimental flux recovery rate for DEX was much higher than that predicted by the linear regressions, likely due to its snow-flake and relatively loose structure of foulant layer which is prone to hydraulic flushing. Though the formation of cake layer is a dominant mechanism for ultrafiltration when foulants size is larger than the membrane cut-off [53], the reported MWCO of the PVC membrane used in this study is 50 kDa but there might still be bigger pores, and some DEX (with colloidal size of 26 nm) might go into the membrane pores and be trapped in the membrane pores and could be flushed out by the backwashing flow. This is evidenced by the CLSM image in Fig. S4c. Meanwhile, HA had bigger colloidal size of 213 nm even though it had wide range of molecular weight (2-500 kDa). During the backwash, the fouling caused by DEX foulants in the pores might be easier to be removed than the porous foulant layer on membrane surfaces. This also implies that our defouling kinetics model is primarily suitable for explaining the role of adhesion force in the cake layer fouling mechanism.

4. Implications

Based on the evaluation of fouling and defouling kinetics of HA, BSA and DEX on PVC membrane during filtration, we presented a universal toolset for analysis of membrane fouling and defouling kinetics using the combined EDLVO theory, Maxwell approach, and particle transport equation. This study have an valuable implication for elucidation and prediction of the filtration performance of ultrafiltration membranes with different foulants and may help the development of antifouling membrane filtration systems. DEX foulant filtration system was an outlier point in the correlation models for defouling kinetics prediction. This outlier implies that this correlation might be better suitable for cake layer fouling mode. To further improve our modeling analysis, other important factors that could affect the fouling and defouling behavior, such as foulant colloidal sizes, fouling layer coverage ratio, foulant layer compressibility under different TMP and shear rate, deserve intensive studies.

Acknowledgement

This work was supported by the NSF Industry/University Cooperative Research Center for Membrane Science, Engineering and Technology [Grant no. IIP1034710]; the National Natural Science Foundation of China project Membrane Fouling Mechanisms Caused by Algogenic Organic Matter (AOM) and its Mitigation during Microalgae Harvesting Process (No. 31672625). The authors also thank Dr. Yuan Xiao (Institute of Hydrobiology, Chinese Academy of Science) for the help in SEM imaging and AFM measurement.

Appendix A. Supplementary material

Supplementary data associated with this article can be found in the online version at doi:10.1016/j.memsci.2018.07.020.

References

- [1] H. Wang, M. Park, H. Liang, S. Wu, I.J. Lopez, W. Ji, G. Li, S.A. Snyder, Reducing ultrafiltration membrane fouling during potable water reuse using pre-ozonation, Water Res. 125 (2017) 42–51.
- [2] W. Yu, N.J. Graham, G.D. Fowler, Coagulation and oxidation for controlling ultrafiltration membrane fouling in drinking water treatment: application of ozone at low dose in submerged membrane tank, Water Res. 95 (2016) 1–10.
- [3] K. Li, T. Huang, F. Qu, X. Du, A. Ding, G. Li, H. Liang, Performance of adsorption pretreatment in mitigating humic acid fouling of ultrafiltration membrane under environmentally relevant ionic conditions, Desalination 377 (2016) 91–98.
- [4] X. Wu, C. Zhou, K. Li, W. Zhang, Y. Tao, Probing the fouling process and mechanisms of submerged ceramic membrane ultrafiltration during algal harvesting under sub- and super-critical fluxes. Sep. Purif. Technol. 195 (2018) 199–207.
- [5] X. Meng, W. Tang, L. Wang, X. Wang, D. Huang, H. Chen, N. Zhang, Mechanism analysis of membrane fouling behavior by humic acid using atomic force microscopy: effect of solution pH and hydrophilicity of PVDF ultrafiltration membrane interface. J. Membr. Sci. 487 (2015) 180–188.
- [6] L. Wang, R. Miao, X. Wang, Y. Lv, X. Meng, Y. Yang, D. Huang, L. Feng, Z. Liu, K. Ju, Fouling behavior of typical organic foulants in polyvinylidene fluoride ultrafiltration membranes: characterization from microforces, Environ. Sci. Technol. 47 (2013) 3708–3714.
- [7] D.T. Myat, M.B. Stewart, M. Mergen, O. Zhao, J.D. Orbell, S. Gray, Experimental and computational investigations of the interactions between model organic compounds and subsequent membrane fouling, Water Res. 48 (2014) 108–118.
- [8] T. Lin, Z. Lu, W. Chen, Interaction mechanisms of humic acid combined with calcium ions on membrane fouling at different conditions in an ultrafiltration system, Desalination 357 (2015) 26–35.
- [9] W. Fu, L. Hua, W. Zhang, Experimental and modeling assessment of the roles of hydrophobicity and zeta potential in chemically modified poly(ether sulfone) membrane fouling kinetics, Ind. Eng. Chem. Res. 56 (2017) 8580–8589.
- [10] J. Chen, M. Zhang, F. Li, L. Qian, H. Lin, L. Yang, X. Wu, X. Zhou, Y. He, B.-Q. Liao, Membrane fouling in a membrane bioreactor: high filtration resistance of gel layer and its underlying mechanism, Water Res. 102 (2016) 82–89.
- [11] B. Tansel, N. Dizge, I.N. Tansel, Analysis of high resolution flux data to characterize fouling profiles of membranes with different MWCO under different filtration modes, Sep. Purif. Technol. 173 (2017) 200–208.
- [12] Y. Sun, Z. Qin, L. Zhao, Q. Chen, Q. Hou, H. Lin, L. Jiang, J. Liu, Z. Du, Membrane fouling mechanisms and permeate flux decline model in soy sauce microfiltration, J. Food Process Eng. 41 (2018) e12599.
- [13] F. Meng, S.R. Chae, A. Drews, M. Kraume, H.S. Shin, F. Yang, Recent advances in

- membrane bioreactors (MBRs): membrane fouling and membrane material, Water Res. 43 (2009) 1489–1512.
- [14] K.J. Hwang, Y.C. Chiang, Comparisons of membrane fouling and separation efficiency in protein/polysaccharide cross-flow microfiltration using membranes with different morphologies, Sep. Purif. Technol. 125 (2014) 74–82.
- [15] A. Mollahosseini, A. Rahimpour, Interfacially polymerized thin film nanofiltration membranes on TiO₂ coated polysulfone substrate, J. Ind. Eng. Chem. 20 (2014) 1261–1268
- [16] F. Qu, H. Liang, J. Zhou, J. Nan, S. Shao, J. Zhang, G. Li, Ultrafiltration membrane fouling caused by extracellular organic matter (EOM) from Microcystis aeruginosa: effects of membrane pore size and surface hydrophobicity, J. Membr. Sci. 449 (2014) 58–66.
- [17] A. Weis, M.R. Bird, M. Nyström, C. Wright, The influence of morphology, hydrophobicity and charge upon the long-term performance of ultrafiltration membranes fouled with spent sulphite liquor, Desalination 175 (2005) 73–85.
- [18] Z. He, S. Kasemset, A.Y. Kirschner, Y.-H. Cheng, D.R. Paul, B.D. Freeman, The effects of salt concentration and foulant surface charge on hydrocarbon fouling of a poly(vinylidene fluoride) microfiltration membrane, Water Res. 117 (2017) 220, 241.
- [19] L.C. Powell, N. Hilal, C.J. Wright, Atomic force microscopy study of the biofouling and mechanical properties of virgin and industrially fouled reverse osmosis membranes, Desalination 404 (2017) 313–321.
- [20] D. Johnson, N. Hilal, Characterisation and quantification of membrane surface properties using atomic force microscopy: a comprehensive review, Desalination 356 (2015) 149–164.
- [21] W.R. Bowen, T.A. Doneva, J.A.G. Stoton, Protein deposition during cross-flow membrane filtration: AFM studies and flux loss, Colloids Surf. B: Biointerfaces 27 (2003) 103–113.
- [22] B. Mi, M. Elimelech, Chemical and physical aspects of organic fouling of forward osmosis membranes, J. Membr. Sci. 320 (2008) 292–302.
- [23] Q. Li, M. Elimelech, Organic fouling and chemical cleaning of nanofiltration membranes: measurements and mechanisms, Environ. Sci. Technol. 38 (2004) 4683–4693.
- [24] K. Xiao, X. Wang, X. Huang, T.D. Waite, X. Wen, Analysis of polysaccharide, protein and humic acid retention by microfiltration membranes using Thomas' dynamic adsorption model, J. Membr. Sci. 342 (2009) 22–34.
- [25] J.-y. Tian, M. Ernst, F. Cui, M. Jekel, Effect of different cations on UF membrane fouling by NOM fractions, Chem. Eng. J. 223 (2013) 547–555.
- [26] W. Zhang, J. Crittenden, K. Li, Y. Chen, Attachment efficiency of nanoparticle aggregation in aqueous dispersions: modeling and experimental validation, Environ. Sci. Technol. 46 (2012) 7054–7062.
- [27] X. Cheng, H. Liang, A. Ding, F. Qu, S. Shao, B. Liu, H. Wang, D. Wu, G. Li, Effects of pre-ozonation on the ultrafiltration of different natural organic matter (NOM) fractions: membrane fouling mitigation, prediction and mechanism, J. Membr. Sci. 505 (2016) 15–25.
- [28] L. Hou, Z. Wang, P. Song, A precise combined complete blocking and cake filtration model for describing the flux variation in membrane filtration process with BSA solution. J. Membr. Sci. 542 (2017) 186–194
- [29] T. Lin, B. Shen, W. Chen, X. Zhang, Interaction mechanisms associated with organic colloid fouling of ultrafiltration membrane in a drinking water treatment system, Desalination 332 (2014) 100–108.
- [30] X. Zhang, Q. Hu, M. Sommerfeld, E. Puruhito, Y. Chen, Harvesting algal biomass for biofuels using ultrafiltration membranes, Bioresour. Technol. 101 (2010) 5297–5304
- [31] K. Xiao, X. Wang, X. Huang, T.D. Waite, X. Wen, Combined effect of membrane and foulant hydrophobicity and surface charge on adsorptive fouling during microfiltration, J. Membr. Sci. 373 (2011) 140–151.
- [32] S. Lee, S. Kim, J. Cho, E.M.V. Hoek, Natural organic matter fouling due to foulant-membrane physicochemical interactions, Desalination 202 (2007) 377–384.

- [33] J.A. Brant, A.E. Childress, Assessing short-range membrane-colloid interactions using surface energetics, J. Membr. Sci. 203 (2002) 257–273.
- [34] P.Y. Toh, B.W. Ng, A.L. Ahmad, D.C.J. Chieh, J. Lim, The role of particle-to-cell interactions in dictating nanoparticle aided magnetophoretic separation of microalgal cells, Nanoscale 6 (2014) 12838–12848.
- [35] S. Ge, M. Agbakpe, Z. Wu, L. Kuang, W. Zhang, X. Wang, Influences of surface coating, UV irradiation and magnetic field on the algae removal using magnetite nanoparticles, Environ. Sci. Technol. 49 (2014) 1190–1196.
- [36] W. Zhang, Nanoparticle aggregation: principles and modeling, in: D.G. Capco, Y. Chen (Eds.), Nanomaterial: Impacts on Cell Biology and Medicine, Springer, Netherlands, Dordrecht, 2014, pp. 19–43.
- [37] M. Elimelech, J. Gregory, X. Jia, Particle Deposition and Aggregation: Measurement, Modelling and Simulation, Butterworth-Heinemann, Oxford, UK, 2013
- [38] X. Wang, M. Zhou, X. Meng, L. Wang, D. Huang, Effect of protein on PVDF ultrafiltration membrane fouling behavior under different pH conditions: interface adhesion force and XDLVO theory analysis, Front. Environ. Sci. Eng. 10 (2016) 12.
- [39] Y.-P. Chin, G. Aiken, E. O'Loughlin, Molecular weight, polydispersity, and spectroscopic properties of aquatic humic substances, Environ. Sci. Technol. 28 (1994) 1952, 1959.
- [40] J. Shao, J. Hou, H. Song, Comparison of humic acid rejection and flux decline during filtration with negatively charged and uncharged ultrafiltration membranes, Water Res. 45 (2011) 473–482.
- [41] C.R. Evanko, D.A. Dzombak, Influence of structural features on sorption of NOManalogue organic acids to goethite, Environ. Sci. Technol. 32 (1998) 2846–2855.
- [42] J. Parsons, Humus chemistry-genesis, composition, reactions, Soil Sci. 135 (1983) 129–130
- [43] A.W. Zularisam, A. Ahmad, M. Sakinah, A.F. Ismail, T. Matsuura, Role of natural organic matter (NOM), colloidal particles, and solution chemistry on ultrafiltration performance, Sep. Purif. Technol. 78 (2011) 189–200.
- [44] K. Radhakrishnan, P. Sivaraman, W.R. Thilagaraj, Removal of color and COD from actual textile effluent by hybrid biosorption and ultrafiltration processes, J. Water Reuse Desalin. 5 (2015) 505–515.
- [45] I.B. Hassan, M. Ennouri, C. Lafforgue, P. Schmitz, A. Ayadi, Experimental study of membrane fouling during crossflow microfiltration of yeast and bacteria suspensions: towards an analysis at the microscopic level, Membranes 3 (2013) 44–68.
- [46] L.D. Tijing, Y.C. Woo, J.-S. Choi, S. Lee, S.-H. Kim, H.K. Shon, Fouling and its control in membrane distillation—a review, J. Membr. Sci. 475 (2015) 215–244.
- [47] F. Zamani, A. Ullah, E. Akhondi, H.J. Tanudjaja, E.R. Cornelissen, A. Honciuc, A.G. Fane, J.W. Chew, Impact of the surface energy of particulate foulants on membrane fouling, J. Membr. Sci. 510 (2016) 101–111.
- [48] S.-E. Wu, N.-J. Lin, C.-Y. Chou, C.-C. Hu, K.-L. Tung, Biofouling mechanism of polysaccharide-protein-humic acid mixtures on polyvinylidene fluoride microfiltration membranes, J. Taiwan Inst. Chem. Eng. (2017).
- [49] M. Zhang, B.-q. Liao, X. Zhou, Y. He, H. Hong, H. Lin, J. Chen, Effects of hydro-philicity/hydrophobicity of membrane on membrane fouling in a submerged membrane bioreactor, Bioresour. Technol. 175 (2015) 59–67.
- [50] L. Song, Flux decline in crossflow microfiltration and ultrafiltration: mechanisms and modeling of membrane fouling, J. Membr. Sci. 139 (1998) 183–200.
 [51] H. Chang, H. Liang, F. Qu, B. Liu, H. Yu, X. Du, G. Li, S.A. Snyder, Hydraulic
- [51] H. Chang, H. Liang, F. Qu, B. Liu, H. Yu, X. Du, G. Li, S.A. Snyder, Hydraulic backwashing for low-pressure membranes in drinking water treatment: a review, J. Membr. Sci. 540 (2017) 362–380.
- [52] E. Akhondi, F. Wicaksana, A.G. Fane, Evaluation of fouling deposition, fouling reversibility and energy consumption of submerged hollow fiber membrane systems with periodic backwash, J. Membr. Sci. 452 (2014) 319–331.
- [53] H. Susanto, H. Arafat, E.M.L. Janssen, M. Ulbricht, Ultrafiltration of polysaccharide–protein mixtures: elucidation of fouling mechanisms and fouling control by membrane surface modification, Sep. Purif. Technol. 63 (2008) 558–565.